The Astrophysical Journal Letters, 829:L35 (6pp), 2016 October 1 doi:10.3847/2041-8205/829/2/L35

A GAP WITH A DEFICIT OF LARGE GRAINS IN THE PROTOPLANETARY DISK AROUND TW Hya

Takashi Tsukagoshi[1], Hideko Nomura[2], Takayuki Muto[3], Ryohei Kawabe[4,10,11], Daiki Ishimoto[2,5], Kazuhiro D. Kanagawa[6], Satoshi Okuzumi[2], Shigeru Ida[7], Catherine Walsh[8,12], and T. J. Millar[9]
[1] College of Science, Ibaraki University, Bunkyo 2-1-1, Mito, Ibaraki 310-8512, Japan; takashi.tsukagoshi.sci@vc.ibaraki.ac.jp
[2] Department of Earth and Planetary Sciences, Tokyo Institute of Technology, 2-12-1 Ookayama, Meguro, Tokyo 152-8551, Japan
[3] Division of Liberal Arts, Kogakuin University, 1-24-2 Nishi-Shinjuku, Shinjuku-ku, Tokyo 163-8677, Japan
[4] National Astronomical Observatory of Japan, 2-21-1 Osawa, Mitaka, Tokyo 181-8588, Japan
[5] Department of Astronomy, Graduate School of Science, Kyoto University, Kitashirakawa-Oiwake-cho, Sakyo, Kyoto 606-8502, Japan
[6] Institute of Physics and CASA*, Faculty of Mathematics and Physics, University of Szczecin, Wielkopolska 15, 70-451 Szczecin, Poland
[7] Earth-Life Science Institute, Tokyo Institute of Technology, 2-12-1 Ookayama, Meguro, Tokyo 152-8550, Japan
[8] Leiden Observatory, Leiden University, P.O. Box 9513, 2300 RA Leiden, The Netherlands
[9] Astrophysics Research Centre, School of Mathematics and Physics, Queen's University Belfast, University Road, Belfast BT7 1NN, UK
[10] SOKENDAI (The Graduate University for Advanced Studies), 2-21-1 Osawa, Mitaka, Tokyo 181-8588, Japan
[11] Department of Astronomy, School of Science, University of Tokyo, Bunkyo, Tokyo 113-0033, Japan
[12] School of Physics and Astronomy, University of Leeds, Leeds LS2 9JT, UK
Received 2016 April 29; revised 2016 August 25; accepted 2016 August 31; published 2016 September 30

ABSTRACT

We report ~3 au resolution imaging observations of the protoplanetary disk around TW Hya at 145 and 233 GHz with the Atacama Large Millimeter/submillimeter Array. Our observations revealed two deep gaps (~25%–50%) at 22 and 37 au and shallower gaps (a few percent) at 6, 28, and 44 au, as recently reported by Andrews et al. The central hole with a radius of ~3 au was also marginally resolved. The most remarkable finding is that the spectral index $\alpha(R)$ between bands 4 and 6 peaks at the 22 au gap. The derived power-law index of the dust opacity $\beta(R)$ is ~1.7 at the 22 au gap and decreases toward the disk center to ~0. The most prominent gap at 22 au could be caused by the gravitational interaction between the disk and an unseen planet with a mass of $\lesssim$1.5 $M_{\rm Neptune}$, although other origins may be possible. The planet-induced gap is supported by the fact that $\beta(R)$ is enhanced at the 22 au gap, indicating a deficit of ~millimeter-sized grains within the gap due to dust filtration by a planet.

Key words: protoplanetary disks – stars: individual (TW Hya)

1. INTRODUCTION

Protoplanetary disks are the birthplaces of planets. The complex structures of protoplanetary disks such as spiral arms, inner holes, and gap and ring, recently reported by high-resolution infrared observations (e.g., Espaillat et al. 2014 and references therein), are believed to be potential evidence of unseen planets in the disk. Most recently, high-resolution observations with Atacama Large Millimeter/submillimeter Array (ALMA) have found multiple gaps and rings in a disk even at submillimeter wavelengths (ALMA Partnership et al. 2015). Since submillimeter emission better traces the midplane density structures than infrared, the gaps and rings are thought to be direct evidence of the absence and enhancement of disk material, and therefore related to the planet formation process. The origin of multiple gaps and rings is still under debate: several theoretical studies predict a formation scenario due to material clearance by planets (Dipierro et al. 2015; Dong et al. 2015; Kanagawa et al. 2015, 2016; Tamayo et al. 2015; Jin et al. 2016), growth and destruction of icy dust aggregates near the snow lines of major volatiles (Zhang et al. 2015; Okuzumi et al. 2016), baroclinic instability triggered by dust settling (Lorén-Aguilar & Bate 2015), or secular gravitational instability (Youdin 2011; Takahashi & Inutsuka 2014).

TW Hya is a 0.8 $M_\odot$ T Tauri star surrounded by a disk at a distance of ~54 pc (e.g., Andrews et al. 2012). Since the disk is almost face-on with an inclination angle of 7° (Qi et al. 2004), TW Hya is one of the best astronomical laboratories to investigate the radial structure of protoplanetary disks. The disk mass has been measured to be $>0.05\,M_\odot$ from HD line observations by the *Herschel Space Observatory*, indicating that it is massive enough to form a planetary system (Bergin et al. 2013). Recently, a gap in the dust emission has been found at 20–30 au by submillimeter and near-infrared observations (Akiyama et al. 2015; Rapson et al. 2015; Debes et al. 2016; Nomura et al. 2016; Zhang et al. 2016), which is possibly associated with the CO snow line (Qi et al. 2013). Most recently, Andrews et al. (2016) reported the existence of multiple, axisymmetric gaps at 1, 22, 37, and 43 au at a spatial resolution of ~1 au. The depth and width of the submillimeter gap at 20–30 au are consistent with clearing by a super-Neptune-mass planet (Nomura et al. 2016). However, additional information on the dust size distribution with comparable spatial resolution is required to address the physical structure of the gap. In this Letter, we report multi-frequency observations of the disk around TW Hya with ALMA to probe the detailed disk structure and the change of dust spectral index across the dust gaps and rings at a spatial resolution of ~3 au.

2. OBSERVATIONS

High-resolution continuum observations at Bands 4 and 6 (145 and 233 GHz) with ALMA were carried out on 2015 December 1 and 2 (2015.A.00005.S). In the observation period, 36 of the 12 m antennas were operational and the antenna configuration was in transition from C36-7 to C36-1, resulting in maximum baselines of 6.5 and 10.4 km for Bands 4 and 6, respectively. We employed the Time Division Mode of the correlator, which is optimized for continuum observations. The correlator was configured to detect dual polarizations in four spectral windows with a bandwidth of 1.875 GHz each,

resulting in a total bandwidth of 7.5 GHz for each observed band. The amplitude and phase were calibrated by observations of J1103-3251, and J1037-2934 was used for absolute flux calibration. The observed passbands were calibrated by 5 minute observations of J1037-2934 and J1107-4449 for Bands 4 and 6, respectively.

The visibility data were reduced and calibrated using the Common Astronomical Software Application (CASA) package, version 4.5.0. After flagging bad data and applying the calibrations for bandpass, complex gain, and flux scaling, the corrected visibilities were imaged by the CLEAN algorithm. The visibilities at Band 6 with *uv* lengths >3000 kλ were flagged out because of significant phase noise. The *uv* sampling for baseline $\lesssim$400 m was particularly sparse along the north–south direction (i.e., *v*-axis of the *uv* coverage), which corresponds to $\lesssim$180 and $\lesssim$300 kλ for Bands 4 and 6, respectively. We have combined Band 6 archival data (2012.1.00422.S), in which the maximum baseline is ~500 kλ, with our Band 6 data after applying a phase shift to account for proper motion and different input phase centers. There were no available short-baseline data at Band 4; hence, only the long-baseline data were used for imaging.

To improve the image fidelity, we performed the iterative self-calibration imaging for each band data using the initial CLEAN image as a model image. The interval time to solve the complex gain was varied from 600 to 90 s for Band 4 and from 1200 to 240 s for Band 6. The resultant images after self-calibration were made by adopting briggs weighting of robust parameters 0.5 and 1.0 for Bands 4 and 6, respectively. We also employed the multiscale clean with scale parameters of [0, 100, 300] and [0, 50, 150] mas for Bands 4 and 6, respectively, for better reconstruction of extended emission. The spatial resolutions of the final images are 88.1 × 62.1 mas with a position angle (PA) of 57.°8 and 75.4 × 55.2 mas with a PA of 38.°0 for Bands 4 and 6, respectively. The noise levels of the Band 4 and 6 images are 12.4 and 28.7 μJy beam^{-1}, respectively.

To deduce the spectral index between the Bands 4 and 6 and to obtain a combined image around the center frequency (190 GHz), we also used the multi-frequency synthesis (MFS) method using all of the corrected visibilities after the iterative self-calibration imaging (*nterm = 2* in CASA *CLEAN* task; see Rau & Cornwell 2011 for the MFS method). Briggs weighting with robust = 0.0 was employed for the deconvolution, and we also employed the multiscale option with scale parameters of 0, 60, and 180 mas. Using the MFS method, we obtain the combined image and the map of the spectral index at 190 GHz. The combined image achieves a better fidelity than the individual images since the observed data are combined to fill the gap in each other's *uv* coverage. The achieved spatial resolution of the combined image is 72.7 × 47.8 mas, with a PA of 52.°9, corresponding to 3.9 × 2.9 au. The noise level is 15.9 μJy beam^{-1}.

3. RESULTS

Figures 1(a) and (b) show the constructed continuum maps at Bands 4 and 6, respectively. Both images show circular multiple gaps and rings even though the resolution of the Band 4 image is ~1.3 times larger than that of Band 6. The total flux densities are 152.0 ± 0.3 and 558.3 ± 0.7 Jy for Bands 4 and 6, respectively.

Figure 1(c) shows the combined image of the Band 4 and 6 data with the MFS method (hereafter MFS image). The MFS image shows circular symmetric multiple gaps and rings. In addition, we have resolved an inner hole with radius ~3 au as predicted from an earlier analysis of the spectral energy distribution (SED; Calvet et al. 2002; Menu et al. 2014). This corresponds to the drop in the brightness temperature of dust continuum map recently found by Andrews et al. (2016). The total flux density integrated over the region with S/N > 10 is 360.3 ± 0.5 mJy at 190 GHz (S/N ~ 150), which agrees well with the previous estimation at submillimeter wavelengths (Qi et al. 2004; Andrews et al. 2012). There is no appreciable deviation from circular symmetry in the gaps, rings, and spectral index α. Ellipsoid fittings of gaps and rings show the deviation between major and minor axes is within the errors ($\lesssim$5%).

To confirm the gap structures, we plot the deprojected radial profile of the continuum emission in the top panel of Figure 2. The flux density is converted to the brightness temperature using the Planck function. There are two prominent gaps at 22 and 37 au, and relatively weak decrements are also seen at 6, 28, and 44 au. These observed features agree with those found by recent high-resolution (~1 au) observations at Band 7 (Andrews et al. 2016). The FWHM and the relative depth are roughly 7 au and 50% for the 22 au gap if the background with a power-law form is assumed, and 3 au and ~20% for the 37 au gap. The depths are deeper than that of the gaps at Band 7 (Andrews et al. 2016), while the widths are comparable. Both the emission at Bands 4 and 6 show comparable brightness temperature inside $R \sim 15$ au, the value of which is consistent with that of the Band 7 emission (Andrews et al. 2016). This result indicates that the disk is (at least moderately) optically thick in this region.

Figure 1(d) shows the spatial variation of the spectral index α (see Equation (2) for its definition). The distribution seems to be axisymmetric, and therefore we make the radial profile of α averaged over the full azimuth angle as shown in Figure 2. The spectral index α radially decreases approaching the disk center. There is a prominent peak around 22 au with $\alpha \sim 3.0$, which coincides well with the position of the gap. The enhancement in α is possible evidence of large grain deficit since α is related to the power-law index of the dust mass opacity if the emission is optically thin. The rapid decrease of α inside the 22 au peak is partly due to increase of optical depth and partly due to decrease of the power-law index of β, namely, the existence of larger dust grains near the central star (see the next section). There seems to be two weak (<10%) bumps at 37 and 44 au that are coincident with the locations of gaps in the intensity profile as for the 22 au gap, implying that there is a correlation between the surface brightness and α.

The error bars in Figure 2 are determined from the standard deviation determined by the azimuthal averaging. This is a conservative way of determining the error because it is the most dominant source of the deviation at >5 au. In fact, the uncertainty map for α produced by CASA shows an error is lower than the standard deviation. The uncertainty in the absolute flux density does not affect the shape of the α profile, but the absolute scale of α. If the accuracy of the absolute flux scale is assumed to be ~10%, the α scale would have an associated error of $\Delta\alpha \sim 0.4$. Therefore the weighted mean value is estimated to be $\langle\alpha\rangle = 2.42 \pm 0.42$, which agrees well

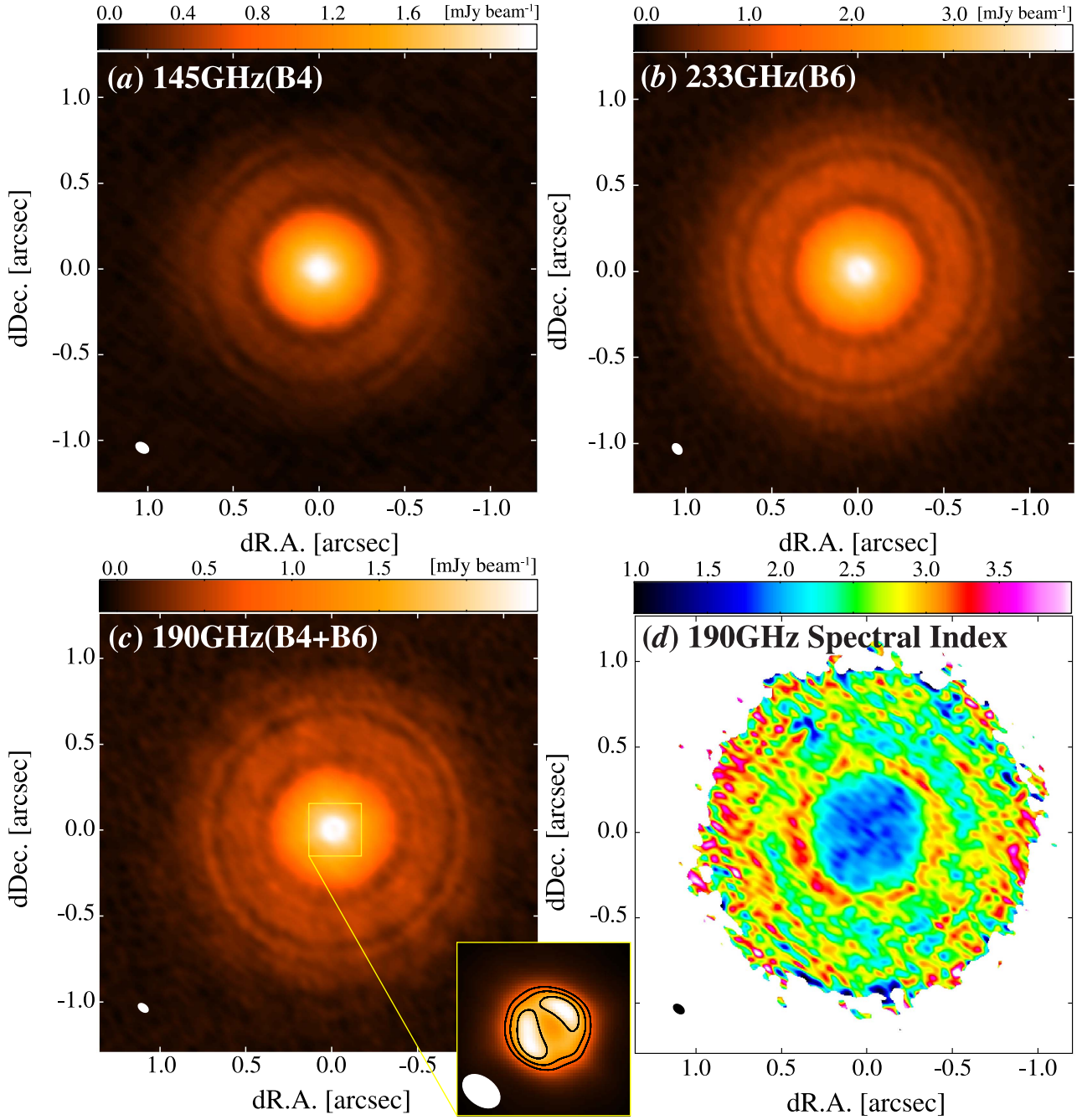

Figure 1. (a) and (b) ALMA continuum images at 145 GHz (Band 4) and 233 GHz (Band 6), respectively. The ellipse at the bottom left corner in each panel shows the synthesized beam. (c) Combined image of Bands 4 and 6 with the MFS method. The inset indicates a close-up view ($0\farcs3 \times 0\farcs3$) for emphasis of the central structure. The contour indicates 130, 140, and 150σ. (d) Spectral index map derived from the MFS method.

with previous measurements for the entire disk (Menu et al. 2014; Pinilla et al. 2014).

4. DISCUSSION

4.1. Radial Profiles of Dust Optical Depth and Opacity β

The intensity $I_\nu(R)$ and the spectral index $\alpha(R)$ are related to the dust temperature $T_d(R)$, the optical depth $\tau_\nu(R)$, and the dust opacity index $\beta(R)$ by

$$I_\nu(R) = B_\nu(T_d(R))(1 - \exp[-\tau_\nu]) \quad (1)$$

and

$$\alpha(R) \equiv \frac{d\log(I_\nu)}{d\log\nu} = 3 - \frac{h\nu}{k_B T_d(R)} \frac{e^{h\nu/k_B T_d(R)}}{e^{h\nu/k_B T_d(R)} - 1} + \beta(R)\frac{\tau_\nu(R)}{e^{\tau_\nu(R)} - 1}. \quad (2)$$

Here, $B_\nu(T)$ is the Planck function, h is Planck's constant, c is the speed of light, and k_B is Boltzmann's constant. The optical depth is assumed to have the form $\tau_\nu(R) = \tau_{190\,\mathrm{GHz}}(R)(\nu/190\,\mathrm{GHz})^\beta$. There are three unknown variables in Equations (1) and (2), which are $T_d(R)$, $\tau_{190\,\mathrm{GHz}}(R)$,

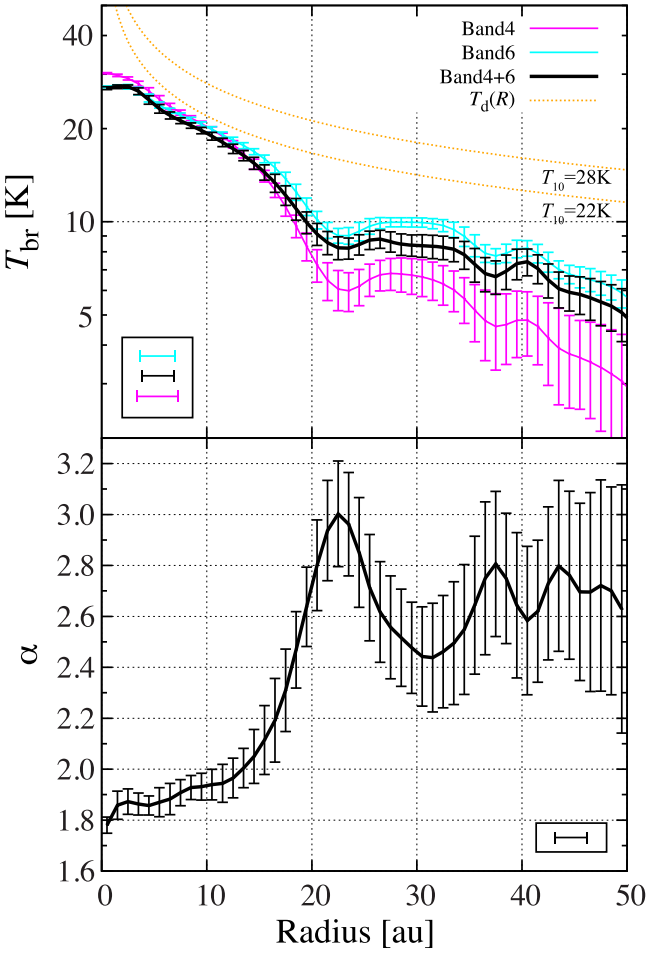

Figure 2. (Top) Radial profiles of the brightness temperature averaged over full azimuthal angle. The black line indicates the MFS combined image, and the lines in magenta and cyan show the Bands 4 and 6 data, respectively. The bars at the bottom left corner show the spatial resolutions. The error bar is determined from the standard deviation through the azimuthal averaging. The orange dashed lines indicate the assumed temperature profile of the dust disk when $T_{10} = 22$ and 28 K with $q = 0.4$. (Bottom) Radial profile of the spectral index α. The resolution is shown at the bottom right corner in the panel. The error bar follows the same manner as the top panel.

and $\beta(R)$. If we assume one of them, we are able to derive the rest of them by using the observation data of $I_\nu(R)$ and $\alpha(R)$. Here, we assume that $T_d(R)$ is given by $T_d(R) = T_{10}(R/10\ \mathrm{au})^{-q}$. We vary T_{10} from 22 to 30 K and q from 0.3 to 0.5 to see how the temperature affects the derived physical quantities. This assumption is based on our fitting to the temperature profile at the disk midplane in Andrews et al. (2012, 2016). The temperature profile models are chosen so that the observed brightness temperature does not exceed the kinetic temperature. The assumed temperature profiles, however, have no great impact on the following conclusions as shown in Figure 3.

Figure 3 shows the radial profiles of $\tau_{190\,\mathrm{GHz}}(R)$ and $\beta(R)$. The errors are estimated in a conservative way in which the combination between the maximum and minimum values of the error bars in the intensity and $\alpha(R)$ profiles is used for determining the maximum range of the error. The disk is optically thin at $R > 15$ au in all the cases and marginally optically thick at $R < 15$ au. This is in contrast with HL Tau (ALMA Partnership et al. 2015; Pinte et al. 2016), where an optically thick region extends out to $R \lesssim 40$ au. We see a prominent drop in the optical depth at $R < 5$ au, which likely corresponds to the inner hole derived from the SED (Calvet et al. 2002) and to the drop in the brightness temperature of the dust continuum map recently found by Andrews et al. (2016). The optical depth profiles have two dips at $R \sim 22$ au and ~37 au. Note that although β can not be determined where the optical thickness is considerably high, the β profile at <15 au is still accessible because τ is of order unity.

Overall, $\beta(R)$ increases from ~0 to ~1.7 with when moving from the disk center to ~20 au, where the disk is marginally optically thick. This implies that sufficient large dust grains ($\gtrsim$ 10 mm) exist at 5–10 au. Radially increasing profiles of $\beta(R)$ are also seen in other T Tauri disks (e.g., Pérez et al. 2012), and compact distribution of the largest grains is suggested in the TW Hya disk, too (Menu et al. 2014).

One of the most remarkable features of the $\beta(R)$ profile is the peak at ~22 au, which corresponds to the location of the gap in the surface brightness profile. This indicates that large dust grains are less abundant within the gap compared to other locations in the disk. We also tentatively see the increase in $\beta(R)$ near the 37 au gap (and perhaps also near the 44 au gap), but further observations with better sensitivity is needed to confirm this.

At $R < 15$ au where $\tau(R) \sim 1$, $\beta(R)$ is derived to be ranging from 0.0 to 0.5, and according to the theoretical calculation of dust mass opacity (Draine 2006), small β value suggests that the power-law index of dust size distribution is very small and and the maximum dust size is large (>a few cm). Also, the result suggests that the column density would be at least an order of magnitude higher than that at the 22 au gap, giving us the column density with an power-law index of <-2. The steep profile is consistent with the previous measurement that large grains should be concentrated toward the inner disk region to reproduce the 9 mm emission (Menu et al. 2014).

The discussions of $\tau_{190\,\mathrm{GHz}}(R)$ and $\beta(R)$ presented here are based on the assumptions of smooth temperature profiles. Observations at additional bands (preferably at lower frequencies) may further constrain $T_d(R)$, $\tau_\nu(R)$ and $\beta(R)$ simultaneously. We note that our results are roughly consistent with the Band 7 observations by Andrews et al. (2016).

4.2. Origin of the Gaps

The enhancement of $\beta(R)$ indicates a deficit of large (millimeter-sized) grains at the gap position. These facts support the scenario that the gap is caused by planet–disk interaction because it is consistent with the picture of dust filtration and trapping due to a planet (Zhu et al. 2012). Using the relationship that connects the gap shape with the planet mass (Kanagawa et al. 2015, 2016), a planet with 1.5 M_{Neptune} may be responsible for the gap, assuming a viscosity parameter $\alpha = 10^{-3}$ and a disk aspect ratio of 0.05 (consistent with the assumption of $T_{10} = 22$ K). We note that similar values are derived from both gap width and depth. This planet mass should be considered as the upper limit since the formula by Kanagawa et al. (2015, 2016) is for the gas gap and the actual dust gap may be wider and deeper than the gas gap due to dust filtration (Zhu et al. 2012).

Alternatively, the multiple ring structures might be related to the snow lines of major volatiles (Zhang et al. 2015; Okuzumi et al. 2016). TW Hya is suggested to have a CO snow line at

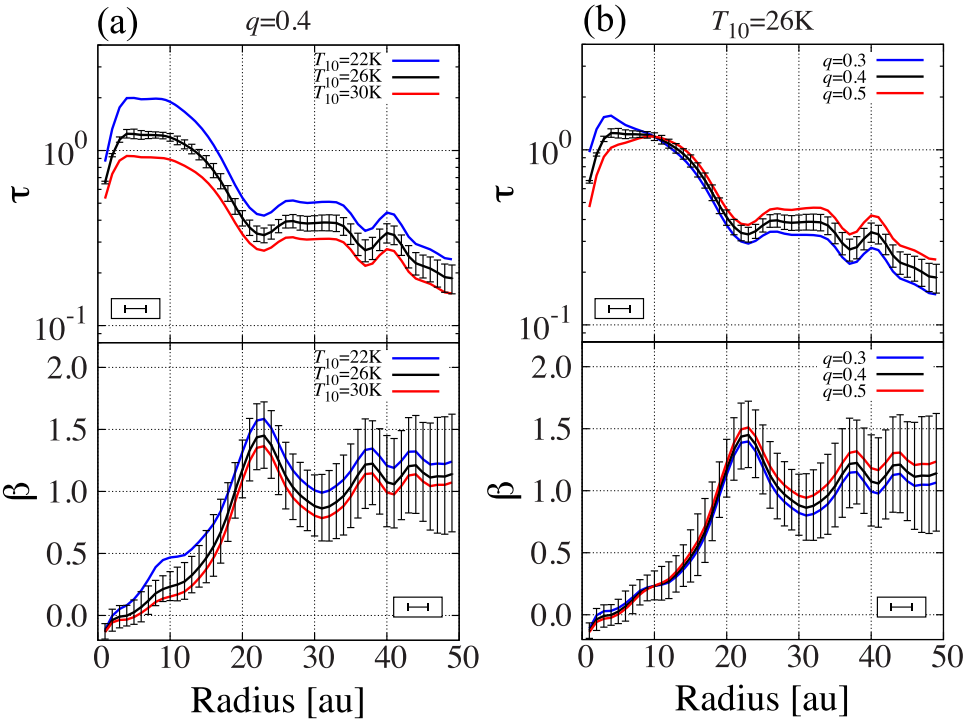

Figure 3. (a) Radial profile of the optical depth at 190 GHz (top) and β (bottom). The cases for $T_{10} = 22$, 26, and 30 K when q is fixed to 0.4 are shown in blue, black, and red lines, respectively. The error bar is shown for the case of $T_{10} = 26$ K representatively. The resolution is shown at the bottom left (top) or bottom right (bottom) corner in the panel. (b) Same as (a), but for checking the dependence on q from 0.3 to 0.5 when T_{10} is fixed to 26 K are shown in blue, black, and red lines, respectively. The error bar is shown for the $q = 0.4$ case representatively.

~30 au (Qi et al. 2013; Schwarz et al. 2016), and our observations identify a bright dust ring near this snow line. This is consistent with the dust ring formation scenario by Okuzumi et al. (2016), in which icy dust aggregates experience sintering, disrupt, and pileup near major snow lines. As noted by Andrews et al. (2016), the 40 au bright ring might correspond to the snow line of N_2, which has a sublimation temperature slightly lower than that of CO. However, the model of Okuzumi et al. (2016) does not predict a strong radial variation of $\beta(R)$, thus not explaining the enhancement of $\beta(R)$ we found near the 20 au dark ring.

The multiple gaps with intervals of 5–10 au beyond the 22 au gap (22, 28, 37, and 44 au) may be reminiscent of dynamical instabilities within the disk such as zonal flow patterns driven by MHD turbulence (Johansen et al. 2009), baroclinic instability driven by dust settling (Lorén-Aguilar & Bate 2015), and/or the secular gravitational instability (Youdin 2011; Takahashi & Inutsuka 2014). Different dynamical processes act under different physical conditions and therefore better constraints on the dust disk physical structure based on high-resolution observations at other bands (e.g., Andrews et al. 2016), and constraints of the density and temperature structures of gas component are essential in determining the origin of such structures.

We thank the referee for many useful comments and critiques which helped improve the contents of this paper. This paper makes use of the following ALMA data: ADS/JAO.ALMA#2015.A.00005.S and ADS/JAO.ALMA#2012.1.00422.S. ALMA is a partnership of ESO (representing its member states), NSF (USA) and NINS (Japan), together with NRC (Canada), NSC and ASIAA (Taiwan), and KASI (Republic of Korea), in cooperation with the Republic of Chile. The Joint ALMA Observatory is operated by ESO, AUI/NRAO and NAOJ. A part of data analysis was carried out on common use data analysis computer system at the Astronomy Data Center of NAOJ. This work is partially supported by JSPS KAKENHI grant numbers 24103504 and 23103004 (TT), 23103005 and 25400229 (HN), 26800106 and 15H02074 (TM), and 16K17661 (SO). K.D.K. was supported by Polish National Science Centre MAESTRO grant DEC- 2012/06/A/ST9/00276. Astrophysics at QUB is supported by a grant from the STFC.

REFERENCES

Akiyama, E., Muto, T., Kusakabe, N., et al. 2015, ApJL, 802, L17
ALMA Partnership, Brogan, C. L., Pérez, L. M., et al. 2015, ApJL, 808, L3
Andrews, S. M., Wilner, D. J., Hughes, A. M., et al. 2012, ApJ, 744, 162
Andrews, S. M., Wilner, D. J., Zhu, Z., et al. 2016, ApJL, 820, L40
Bergin, E. A., Cleeves, L. I., Gorti, U., et al. 2013, Natur, 493, 644
Calvet, N., D'Alessio, P., Hartmann, L., et al. 2002, ApJ, 568, 1008
Debes, J. H., Jang-Condell, H., & Schneider, G. 2016, ApJL, 819, L1
Dipierro, G., Price, D., Laibe, G., et al. 2015, MNRAS, 453, L73
Dong, R., Zhu, Z., Rafikov, R. R., & Stone, J. M. 2015, ApJL, 809, L5
Draine, B. T. 2006, ApJ, 636, 1114
Espaillat, C., Muzerolle, J., Najita, J., et al. 2014, in Protostars and Planets VI, ed. H. Beuther et al. (Tucson, AZ: Univ. Arizona Press), 497
Hogerheijde, M. R., Bekkers, D., Pinilla, P., et al. 2016, A&A, 586, A99
Jin, S., Li, S., Isella, A., Li, H., & Ji, J. 2016, ApJ, 818, 76
Johansen, A., Youdin, A., & Klahr, H. 2009, ApJ, 697, 1269
Kanagawa, K. D., Muto, T., Tanaka, H., et al. 2015, ApJL, 806, L15
Kanagawa, K. D., Muto, T., Tanaka, H., et al. 2016, PASJ, 68, 43
Lin, D. N. C., & Papaloizou, J. 1979, MNRAS, 186, 799
Lorén-Aguilar, P., & Bate, M. R. 2015, MNRAS, 453, L78
Menu, J., van Boekel, R., Henning, T., et al. 2014, A&A, 564, A93
Nomura, H., Tsukagoshi, T., Kawabe, R., et al. 2016, ApJL, 819, L7
Okuzumi, S., Momose, M., Sirono, S.-i., Kobayashi, H., & Tanaka, H. 2016, ApJ, 821, 82

Pérez, L. M., Carpenter, J. M., Chandler, C. J., et al. 2012, ApJL, 760, L17
Pinilla, P., Benisty, M., Birnstiel, T., et al. 2014, A&A, 564, A51
Pinte, C., Dent, W. R. F., Ménard, F., et al. 2016, ApJ, 816, 25
Qi, C., Ho, P. T. P., Wilner, D. J., et al. 2004, ApJL, 616, L11
Qi, C., Öberg, K. I., Wilner, D. J., et al. 2013, Sci, 341, 630
Rapson, V. A., Kastner, J. H., Millar-Blanchaer, M. A., & Dong, R. 2015, ApJL, 815, L26
Rau, U., & Cornwell, T. J. 2011, A&A, 532, A71
Schwarz, K. R., Bergin, E. A., Cleeves, L. I., et al. 2016, ApJ, 823, 91
Takahashi, S. Z., & Inutsuka, S.-i 2014, ApJ, 794, 55
Tamayo, D., Triaud, A. H. M. J., Menou, K., & Rein, H. 2015, ApJ, 805, 100
van Leeuwen, F. 2007, A&A, 474, 653
Youdin, A. 2011, ApJ, 731, 99
Zhang, K., Bergin, E. A., Blake, G. A., et al. 2016, ApJL, 818, L16
Zhang, K., Blake, G. A., & Bergin, E. A. 2015, ApJL, 806, L7
Zhu, Z., Nelson, R. P., Dong, R., Espaillat, C., & Hartmann, L. 2012, ApJ, 755, 6